Charge density wave, enhanced mobility, and large nonsaturating magnetoresistance across the magnetic states of $HoNiC_2$ and $ErNiC_2$

Kamil K. Kolincio [1,*] Marta Roman [2,3] Fabian Garmroudi [2] Michael Parzer [2] Ernst Bauer [2] and Herwig Michor [2]

[1] *Faculty of Applied Physics and Mathematics, Gdansk University of Technology, Narutowicza 11/12, 80-233 Gdansk, Poland*

[2] *Institute of Solid State Physics, TU Wien, Wiedner Hauptstrasse 8–10, A-1040 Wien, Austria*

[3] *Institute of Physics and Applied Computer Science, Faculty of Applied Physics and Mathematics and Advanced Materials Center, Gdansk University of Technology, Narutowicza 11/12, 80-233 Gdansk, Poland*

(Received 27 October 2023; revised 22 December 2023; accepted 22 January 2024; published 23 February 2024)

We report on magnetotransport and thermoelectric properties of two ternary carbides $HoNiC_2$ and $ErNiC_2$ hosting both charge density wave and long-range magnetic order. In the charge density wave state, both compounds show relatively large magnetoresistance MR $\approx 150\%$ in $HoNiC_2$ and $\approx 70\%$ in $ErNiC_2$ at a magnetic field of 9 T and temperature as low as 2 K. This positive field-linear magnetoresistance shows no signatures of saturation. Our combined analysis of diagonal and off-diagonal transport responses reveals electronic mobility values on the order of 10^3 cm^2 V^{-1} s^{-1} at 2 K. Both the elevated mobility and related enhanced magnetoresistance persist in the zero-field antiferromagnetic ground state and survive the field-induced crossovers through metamagnetic to field-aligned ferromagnetic states. The robustness of the high-mobility Fermi surface pockets across the magnetically ordered states suggests that the charge density wave is not suppressed but coexists with long-range magnetism in the entire dome of the magnetically ordered states.

DOI: 10.1103/PhysRevB.109.075154

I. INTRODUCTION

The charge density wave (CDW) is a periodical modulation of the electron density, coupled to a periodical lattice distortion and induced by a Peierls instability of a low-dimensional electron gas [1,2]. One of the characteristic features represented by materials showing a Peierls transition is a nesting of the Fermi surface (FS). A theoretical model, based on an ideal one-dimensional metallic chain, predicts the formation of a CDW gap, and thus a removal of the entire FS [2]. This is closely followed in some of the CDW materials such as $(TaSe_4)_2I$ [3], molybdenum bronzes [4–6], or organic conductors [7,8] showing pronounced metal-semiconductor transitions. However, in a vast majority of materials undergoing a Peierls transition, the nesting is not complete and a metal-metal transition is observed at the onset of the CDW state [9–11], as seen in canonical CDW systems such as $NbSe_3$ [12,13]. In the latter case, the remaining pockets of the Fermi surface can become a source of low-effective-mass electronic carriers with an enhanced mobility leading to improved thermoelectric performance [14,15] and pronounced magnetotransport responses [16–18].

Even a broader horizon of potential applications opens if the high mobility of conduction carriers can be combined with long-range magnetism [19,20]. A broadly explored route to maintain both of them in a solid leads through the presence of peculiarities such as Dirac cones, Weyl nodes, or other sharp features in the electronic structure [21], yet the number of materials exhibiting both of them is limited [22]. Another path leads through the coexistence of CDW and magnetism. A limitation of this route is a tendency to competition between these orderings often leading to the suppression of one of them [23–25] with a particularly strong destructive interaction between charge density wave and ferromagnetism. Nonetheless, there are several systems in which both entities—CDW and long-range magnetic order—do coexist [26–29].

The realization of such a scenario has been reported for the family of ternary carbides represented by a general formula $RNiC_2$, where R stands for a rare-earth ion. Charge density wave–related structure modulation observed in the early lanthanide-based $RNiC_2$ is represented by the commensurate or nearly commensurate wave vector $q_1 = (0.5,\ 0.5 + \eta,\ 0)$ [30]. In $NdNiC_2$ and $GdNiC_2$, despite a partial CDW suppression, it coexists with antiferromagnetic (AFM) order, but it is destroyed by a field-aligned ferromagnetic state [31–33]. This suppression effect is also relevant for $SmNiC_2$, where the ground state is of a purely ferromagnetic character [34,35]. In $RNiC_2$ consisting of heavier R ions, the charge density wave state evolves to the commensurate state with $q_2 = (0.5,\ 0.5,\ 0.5)$ [36,37], appearing already at and above room temperature [38]. In contrast to the q_1 state, which only breaks the translation symmetry, q_2 inflicts more pronounced structural implications, with the reduction of the point symmetry from $mm2$ to m [37,39]. Large differences are also visible in the nesting properties, as the q_2 state has been found to unveil the high-mobility pockets, not seen in $RNiC_2$ exhibiting a q_1-CDW state. The resulting strong magnetoresistive features have been observed in both nonmagnetic $YNiC_2$ and $LuNiC_2$ [40] as well as in $TmNiC_2$ [41], which additionally shows AFM order at low temperature [42]. Moreover, the q_2-type charge density wave in $TmNiC_2$, together

*kamil.kolincio@pg.edu.pl

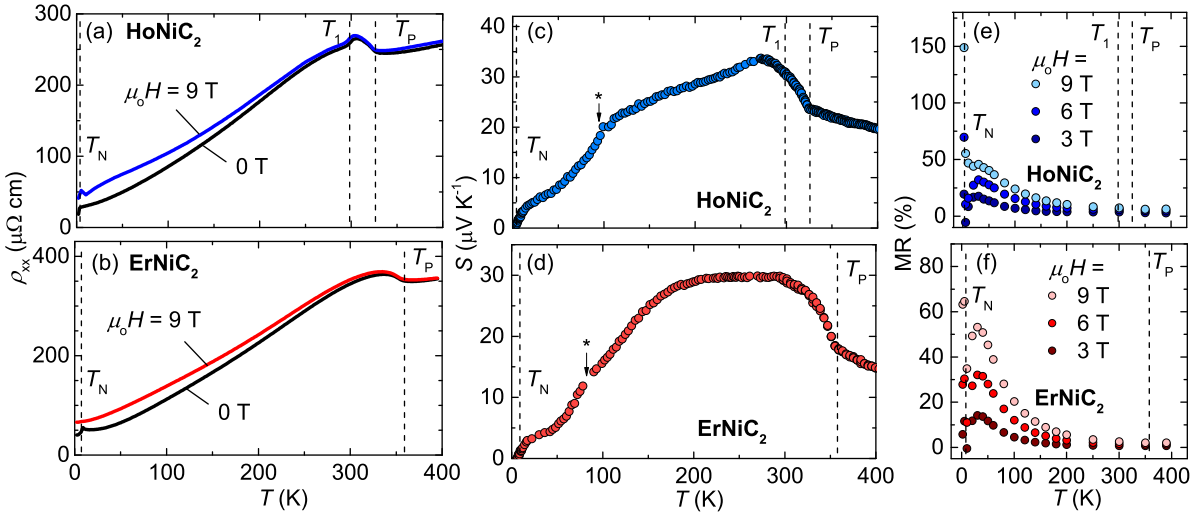

FIG. 1. (a), (b): Temperature dependence of resistivity for $HoNiC_2$ (a) and $ErNiC_2$ (b) measured under zero-field condition (black) and under an external magnetic field of 9 T (blue and red curves, respectively). (c), (d): Temperature-dependent thermopower for $HoNiC_2$ (c) and $ErNiC_2$ (d). The inflections marked with asterisks are attributed to the measurement setup artifact observed previously in Ref. [43]. (e), (f): Magnetoresistance at $\mu_0 H = 9$ T as a function of temperature for $HoNiC_2$ (e) and $ErNiC_2$ (f). The specific temperatures T_P, T_1, and T_N are marked with dashed vertical lines. No demagnetization correction has been applied here.

with high-mobility pockets, has been suggested not only to coexist with antiferromagnetism, but also to be robust against the field-induced metamagnetic and field-aligned ferromagnetic transitions [41]. This finding inspired us to investigate the galvanomagnetic and thermoelectric properties of $HoNiC_2$ and $ErNiC_2$, to verify the relevance of the same scenario in these compounds, in which the common modulation vector q_2 heralds the close similarities in their electronic structure and Fermi surface nesting conditions.

II. EXPERIMENTAL

The polycrystalline samples were synthesized using a two-step approach: first, pure elements (Ho, Er, and Ni 99.99%; C 99.999%) in appropriate proportions were melted in a radio frequency induction furnace under protective 99.9999% Ar atmosphere and then annealed in evacuated quartz ampules at 900 °C for one week. The sample composition and purity has been confirmed with powder x-ray diffraction using an Aeris powder diffractometer from Malvern Panalytical. A commercial Quantum Design Physical Properties Measurement System (PPMS) was used for magnetization and transport experiments. Magnetization measurements were conducted using the vibrating sample magnetometer (VSM) option. A conventional four-probe technique was used for electrical resistivity measurements. Thin gold wires, serving as electrical contacts, were attached to the polished sample surface using 4922N DuPont silver paint. The magnetic field for Hall effect and magnetoresistance measurements was applied perpendicularly to the electric current. The measured transverse voltage in the Hall experiment was collected with reversal orientation of applied field and antisymmetrized to remove the spurious remainder of the longitudinal signal. The demagnetization correction, based on sample shape [44], has been applied to the values of magnetic fields. For low temperatures, the Seebeck coefficient was measured in a helium-bath cryostat, employing the seesaw heating method as described in Ref. [45]. For every measurement point, the sample is heated on both sides alternatingly to cancel out spurious voltage contributions. The temperature difference is measured using two chromel-constantan thermocouples, which are thermally and electrically connected to the sample. Above room temperature, the thermopower was measured applying the slope method, as described in Refs. [46,47]. Type R thermocouples were used and were electrically and thermally connected to the sample to measure $dS(T)/dT$ applying a dynamic temperature gradient for each measurement point.

III. RESULTS AND DISCUSSION

A. Resistivity and thermopower

Figures 1(a)–1(d) depict the temperature-dependent transport and thermopower properties of $HoNiC_2$ and $ErNiC_2$. Resistivity ρ_{xx} measured under a zero-field condition and under an applied external magnetic field of 9 T is displayed in panels (a) and (b), while thermopower is displayed in panels (c) and (d).

Both compounds share a qualitatively similar behavior. The pronounced anomalies associated with Peierls transitions are simultaneously observed by both techniques at $T_P = 325$ K and 358 K for $HoNiC_2$ and $ErNiC_2$, respectively. In the resistivity curves, they are imposed on a generally metallic course with ρ_{xx} decreasing as the temperature is lowered. Peierls transitions are also manifested by the significant increase of the thermopower $S(T)$ at T_P, contrasting the weak temperature dependence at higher temperatures. The anomalies seen in $\rho_{xx}(T)$ and $S(T)$ indicate a decrease of carrier concentration due to opening of a CDW gap in a part of the Fermi surface. Thermopower remains positive in the entire temperature range, indicating a majority of holes, and shows a broad maximum in the charge-ordered states, attaining values up to 30 $\mu V\,K^{-1}$, characteristic for semimetals such as

Sb [48], Bi [49], or TaAs [50]. While the character of $S(T)$ curves resembles the behavior seen in $SmNiC_2$, also showing a broad maximum below T_P [51], the magnitude of the thermopower peak in this compound ($\approx 7\ \mu V\,K^{-1}$) is significantly weaker than in $HoNiC_2$ and $ErNiC_2$. The positive sign of thermopower indicates that an incorrect sign convention has been used to describe the Hall effect in previous reports [38,41,52,53] on $RNiC_2$.

The transition temperatures are in a measurable agreement with a previous report on polycrystalline samples [38], yet T_P found here is significantly higher than in a $HoNiC_2$ single crystal ($T_P = 305$ K) [36]. As shown in Fig. 1(a), at $T_1 = 291$ K, the resistivity of this compound exhibits additional inflections. The anomaly at this temperature was previously attributed to a lock-in transition [38]. Interestingly, while this feature is seen in polycrystalline samples synthesized by different techniques, it was not observed in the recent report based on a single crystal, where only a single transition has been reported [36]. This contrast between our polycrystalline samples and single crystals, which were extracted by Maeda *et al.* [36] from the surface of arc-melted ingots and reported to be twinned, suggests the presence of another degree of freedom. Mechanical strain may therefore play a role in the subtle interplay between the electronic structure and crystallographic lattice.

In both materials, the antiferromagnetic transitions (at Néel temperatures $T_N \approx 2.8$ K and 8.5 K for $HoNiC_2$ and $ErNiC_2$, respectively [54–56]) are reflected in both resistivity and thermopower curves. The $S(T)$ curves, on the way from a broad maximum located below T_P and near-zero thermopower value observed at 2 K, show visible inflections at T_N. Simultaneously, the resistivity drop is seen at the onset of the magnetically ordered state. This decrease is quantified as the ratio of resistivity above and below T_N, given by Eq. (1):

$$\mathrm{RD} = \frac{\rho_{xx}(T \to +T_N) - \rho_{xx}(T = 2\ \mathrm{K})}{\rho_{xx}(T = 2\ \mathrm{K})}. \tag{1}$$

The values of $\Delta\rho_{xx} = 0.37$ in $HoNiC_2$ and 0.27 in $ErNiC_2$ are smaller than the corresponding quantity RD = 0.50, 0.72, and 0.90 for $NdNiC_2$, $GdNiC_2$, and $SmNiC_2$ [32,34,57]. In these early lanthanide-based compounds the CDW has been found to be either partially suppressed at the onset of the AFM state in $NdNiC_2$ and $GdNiC_2$ [31] or completely destroyed in the ferromagnetic state of $SmNiC_2$ [34,35]. The relatively small RD in $HoNiC_2$ and $ErNiC_2$ is similar to the value found in $TmNiC_2$ (0.43) [41], where CDW was suggested to coexist with long-range magnetism. Our result also corroborates the recent report based on x-ray diffraction [36], confirming the robustness of the q_2-CDW against the antiferromagnetic ordering in $HoNiC_2$ and $ErNiC_2$.

B. Magnetoresistance

Similarly to Y-, Lu-, or Tm-based $RNiC_2$ compounds, the application of an external magnetic field significantly increases the electric resistivity in the CDW state of $HoNiC_2$ and $ErNiC_2$, as shown in panels (a) and (b) of Fig. 1, respectively. This effect is more pronounced in $HoNiC_2$ than in the case of $ErNiC_2$. For clarity, in panels (e) and (f) of Fig. 1, we show the thermal dependence of the magnetoresistance (MR) which is defined as the ratio of the field-induced change of the resistivity to its zero-field value, expressed in percent:

$$\mathrm{MR} = \frac{\rho_{xx}(B) - \rho_{xx}(B = 0)}{\rho_{xx}(B = 0)} \times 100\%. \tag{2}$$

In $HoNiC_2$, and to a lesser extent also in $ErNiC_2$, a small yet finite magnetoresistance is observed in the high-temperature state. In both compounds, the positive MR becomes visibly enhanced upon entering the charge-ordered state and keeps increasing upon lowering the temperature. This trend is locally interrupted by a sharp minimum located at the vicinity of T_N, signaling the emergence of a negative MR component. At the lowest temperature, the positive term prevails again, and the overall MR reaches 150% for $HoNiC_2$ and 70% for $ErNiC_2$ at $T = 2$ K and $\mu_0 H = 9$ T. From the coincidence of the positive MR enhancement with the Peierls transition, one can conclude that this transport response is related to the reconstruction of the Fermi surface caused by q_2-CDW. Similar mechanisms are known to be realized in canonical CDW systems such as transition metal chalcogenides [58–60], molybdenum [61–64], and tungsten bronzes [16,65–67] with imperfect nesting and small pockets containing high-mobility electrons or holes as elements of the reconstructed Fermi surface. This scenario has also been proposed for other $RNiC_2$ [40,41] with q_2-type CDW, showing comparable magnetoresistance responses.

The presence of a negative MR term is a common feature of magnetic materials. When accompanying the transition toward the magnetically ordered state, it is typically related to the rapid quenching of spin disorder scattering by the application of magnetic field. The prime example of this effect is the case of manganese oxide materials [68,69] with magnetic field changing the conduction character from semiconductor-type to metallic. In the early lanthanide-based $RNiC_2$, however, the negative MR has been found to be significantly enhanced due to partial or complete suppression of CDW. In such a case, restoring of the high-temperature Fermi surface, previously decomposed by CDW gap formation, increases the number of conduction carriers and thus decreases the resistivity. This avalanche effect is, however, observed in neither $HoNiC_2$ or $ErNiC_2$.

To obtain a more detailed picture and to distinguish the roles played by subsequent magnetoresistance terms, we have analyzed the magnetic field dependence of resistivity. MR(B) for $HoNiC_2$ and $ErNiC_2$ are shown in panels (a) and (b) of Fig. 2. The overall behavior of magnetoresistance in both compounds exhibits qualitative similarities. In the paramagnetic state, the low-field limit of MR(B) shows a quasiparabolic character, which evolves into a linear field dependence at elevated B. A negative term develops as the temperature approaches T_N, and within the dome of the ordered state, inflections are observed at fields corresponding to magnetic crossovers. At high B, in the field-aligned state, the negative magnetoresistance is overcome by the positive term. In this limit, the overall MR(B) regains the linear character with no saturation up to $\mu_0 H = 9$ T. While this stands in contrast to $NdNiC_2$ and $GdNiC_2$, where the field-induced metamagnetic and ferromagnetic transitions lead to a strong negative MR, the result found in $HoNiC_2$ and $ErNiC_2$ is similar to the case of $TmNiC_2$, where the persistence of large

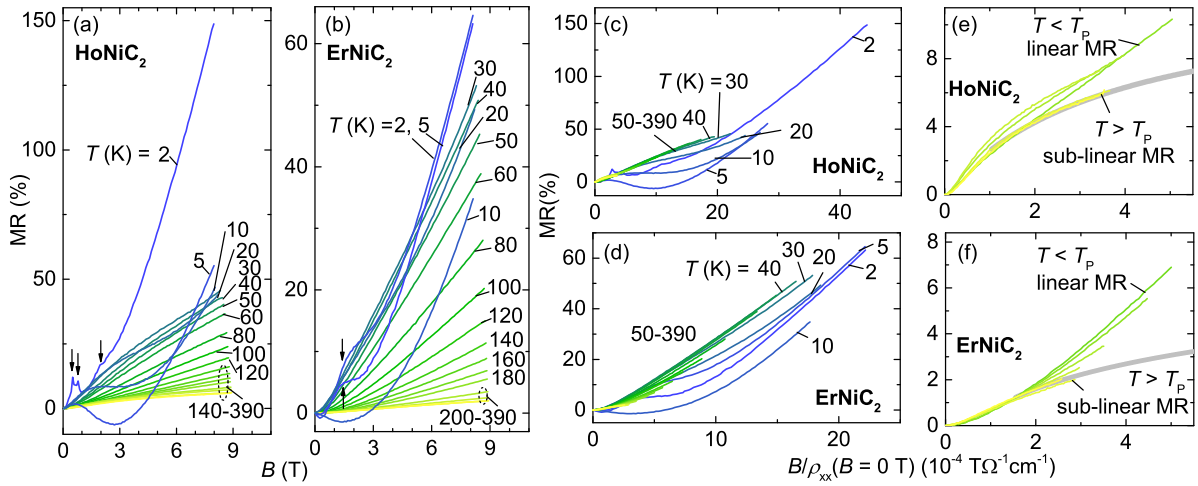

FIG. 2. (a), (b): Field dependence of magnetoresistance measured at constant temperatures in $HoNiC_2$ (a) and $ErNiC_2$ (b). Arrows mark the field-induced phase transitions toward metamagnetic and field-induced ferromagnetic state, reported in Ref. [55]. (c)–(f): Kohler scaling of magnetoresistance. Panels (c) and (d) show the entire temperature range for $HoNiC_2$ and $ErNiC_2$, respectively, while panels (e) and (f) depict the expanded view of the plots corresponding to temperatures from the vicinity of T_P. Gray line serving as a guide to the eye is the extension of the plots at temperatures above charge density wave transition. Identical temperature-color scheme, with colors varying from yellow for $T = 390$ K to dark blue for $T = 2$ K, is maintained across all the panels.

positive MR across the magnetic states has been proposed to result from the robustness of the CDW within the entire dome of the magnetically ordered state [41].

While discussing the high-field limit of the magnetoresistance, it is worth noticing that the linear MR character is often observed in metallic CDW systems. Two mechanisms have been proposed as a possible origin. One is based on sharp turns taken by charge carriers, due to a rough curvature of the partially nested Fermi surface [70]. The second model anticipates a large enhancement of electron scattering from CDW order parameter fluctuations in specific "hot spot" parts of the Fermi surface [71]. Because of the lack of significant disorder and relatively large carrier concentration even in the nested state, one can directly exclude the two most general linear magnetoresistance models—classical [72] and quantum [73,74], respectively. However, one cannot entirely exclude the most simplistic scenario, in which the linear MR term stems from the mixing of the saturating and nonsaturating signals from Fermi surface fragments of closed and open k-space geometry, respectively [75].

A powerful tool for the discussion of magnetoresistance is given by the semiclassical Kohler's scaling. Provided that the material possesses a single conduction channel, together with field-independent and isotropic scattering rates, this model predicts all the plots:

$$\mathrm{MR} = f(\omega_c\tau) = f\left(\frac{B}{\rho_{xx}(B=0)}\right), \tag{3}$$

where ω_c is cyclotron frequency and τ is relaxation time, to collapse into a single curve. Thus, this scaling is a sensitive probe of the evolution of both the electronic structure and the scattering processes. Either of these factors violates the Kohler's rule conditions and thus generates the deviation from the common $\mathrm{MR}(\frac{B}{\rho_{xx}(B=0)})$ trend. A partial limitation of the usability of this model in magnetic systems stems from the fact that the magnetic moments, fluctuating or long-range ordered, respond to an external field, resulting in the field dependence of spin-dependent scattering rate. In the materials under study, however, the magnetic order develops at relatively low temperatures, which, together with paramagnetic Curie-Weiss temperatures being at the order of $|\theta_{CW}| \approx 10$ K for $HoNiC_2$ and ≈ 50 K for $ErNiC_2$ [55], opens the possibility to use the Kohler's approach at least in the limit of high and moderate temperatures, where the magnetic correlations are weak and have a negligible impact on the scattering.

The Kohler's scaling of magnetoresistance for $HoNiC_2$ and $ErNiC_2$ is presented in Figs. 2(c) and 2(d), respectively. Two features are visible already at a first glance in both compounds: the plots show similar courses, yet with pronounced deviations at certain temperatures. Panels (e) and (f) of Fig. 2 detail the high-temperature limit and the vicinity of T_P with an expanded view. At elevated temperatures, above the charge-ordering point, the magnetoresistance curves are sublinear and tend to saturate at high magnetic fields. A gray shading is added in these plots to emphasize this tendency. The magnetoresistance character changes below T_P, where it evolves into nonsaturating behavior, quadratic in the low-field limit and linear at higher B. This is a first violation of the Kohler's rule, which is followed by another, yet less pronounced one: the subsequent plots obtained at lower temperature move higher and higher in the vertical axis. While these plots share qualitatively similar character, they do not overlap. Finally, at temperatures below ≈ 50 K, the plots start to deviate in the opposite direction, due to the emergence of the negative magnetoresistance term that is the most pronounced in the vicinity of and within the magnetically ordered state. Interestingly, when the magnetic field quenches spin disorder, overcoming the negative MR in the field-induced ferromagnetic state, the high-B magnetoresistance regains the character from moderate temperatures. The curves in the high-field limit become parallel to the general trend, indicating that the

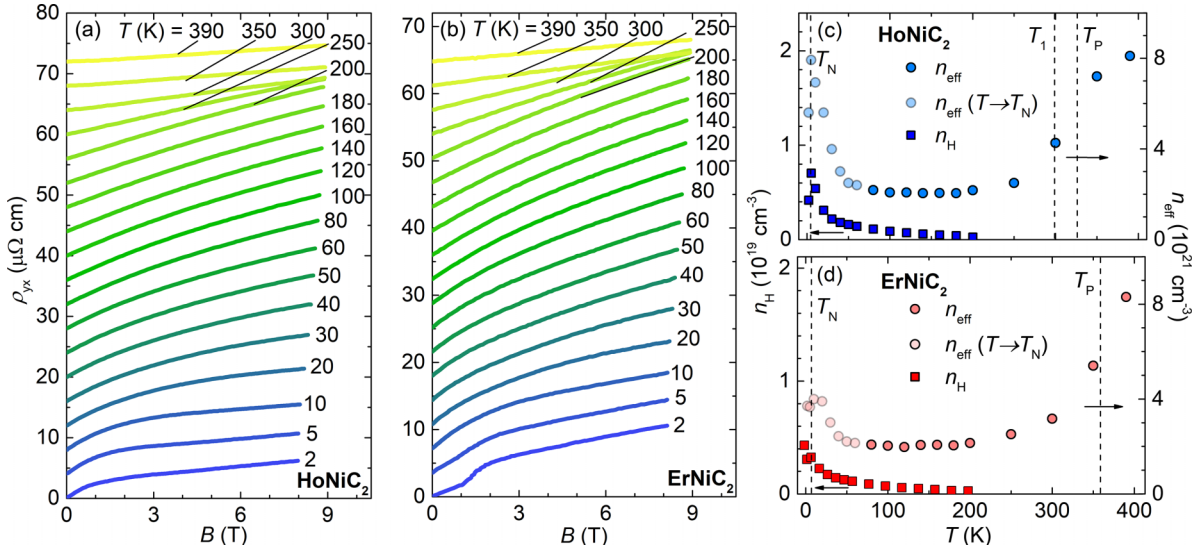

FIG. 3. (a), (b): Field dependence of Hall resistivity in $HoNiC_2$ (a) and $ErNiC_2$ (b). For clarity, the plots corresponding to temperatures higher than 2 K have been shifted vertically. The temperature-color scheme, with colors varying from yellow for $T = 390$ K to dark blue for $T = 2$ K, is identical in panels (a) and (b). (c), (d): Temperature dependence of effective carrier concentration n_{eff}, obtained from high-field limit of $\rho(B)$, using Eq. (6) (circles), high-mobility pocket carrier concentration n_{H} obtained using Eq. 10 (squares) in $HoNiC_2$ (c) and $ErNiC_2$ (d). Shaded circles represent the values of n_{eff} obtained at temperatures close to the magnetic ordering, where Hall resistivity may contain a significant anomalous contribution. Dashed vertical lines mark the subsequent charge density wave and magnetic transitions.

same mechanism responsible for positive magnetoresistance is present both in the paramagnetic-CDW and the magnetic states. Because this nonsaturating, linear MR term appears to be related to the charge density wave as it onsets at the Peierls transition, this result suggests that the CDW coexists not only with antiferromagnetism but also with field-induced metamagnetic and ferromagnetic states.

We note that the presence of CDW-independent electronic structure peculiarities such as Weyl nodes has been predicted to be located close to Fermi energy in $GdNiC_2$, being a member of the $RNiC_2$ family, and $NdRhC_2$, $GdCoC_2$ with the same crystal structure [76]. If such features occurred also in $HoNiC_2$ and $ErNiC_2$, they could partially contribute to the enhanced mobility and magnetoresistance response [77], in addition to its amplification in the CDW state. This possibility, however, even if relevant, does not obstruct tracking of the charge density wave across the magnetic phase diagram. The magnetoresistance behavior of the compounds studied here differs significantly from the one observed in $GdNiC_2$, for which the Weyl-type features have been forecast, and which yet shows no positive MR in the CDW state, as other $RNiC_2$ with q_1-type CDW. This suggests that the large responses seen in $HoNiC_2$ and $ErNiC_2$ are likely not associated to the topology of the pristine, un-nested Fermi surface, but are rooted at the pockets unveiled by imperfect nesting. Furthermore, our analysis shows that it is not only the magnitude but also the character of the high-field magnetoresistance that reflects the presence of the CDW state. The Peierls transition changes the magnetoresistance from weak and saturating as seen at $T > T_{\text{P}}$ to nonsaturating with exponent η in MR $\sim B^{\eta}$ close to unity as observed at $T < T_{\text{P}}$ (see Supplemental Material [78] for more details). Therefore, the presence of the latter linear term marks the existence of Fermi surface nesting and thus of CDW.

C. Hall effect

The charge density wave state is intimately related to the electronic structure; the gap opened at the Fermi level results in a significant reduction of free electronic carrier concentration. If the related decomposition of the Fermi surface is not complete, high-mobility electron and/or hole pockets remain, giving rise to an enhanced MR response. Therefore, exploring the carrier concentration and mobility via the Hall effect not only supports the analysis of elevated magnetoresistance but also provides an (indirect) probe of the CDW state and its relation to magnetism.

The field dependence of Hall resistivity $\rho_{yx}(B)$ in $HoNiC_2$ and $ErNiC_2$ is plotted in panels (a) and (b) of Fig. 3, respectively. At high temperatures, the Hall resistivity is an almost linear function of magnetic field. Upon cooling across the Peierls transition, its B dependence gradually becomes steeper, simultaneously developing a more and more pronounced nonlinearity. While the nonlinear behavior of Hall resistivity is a typical feature of a multiband material comprising multiple conduction channels with different effective masses and mobilities, both $HoNiC_2$ and $ErNiC_2$ exhibit long-range magnetic ordering, which can also partially account for such a transport response. In magnetic materials, one has to consider two terms contributing to the Hall resistivity [79]:

$$\rho_{xy} = \rho_{xy}^{O}(B) + \rho_{xy}^{A}(M). \tag{4}$$

The first one, ρ_{xy}^{O}, is the ordinary Hall counterpart associated to the cyclotron motion of conduction carriers. This term depends solely on the magnetic field; in single-band systems ρ_{xy}^{O} is a linear function of B with a slope that is inversely proportional to the carrier concentration, while in multiband systems it becomes sensitive also to the carrier mobilities. In

a two-band conduction picture, the field dependence of the ordinary Hall coefficient is described by the formula containing both hole and electron concentrations and mobilities, n_h, n_e, μ_h, μ_e, respectively [80]:

$$\rho_{yx}^{O} = \frac{1}{e}\frac{n_h\mu_h^2 - n_e\mu_e^2 + (n_h - n_e)\mu_e^2\mu_h^2B^2}{(n_h\mu_h + n_e\mu_e)^2 + (n_h - n_e)^2\mu_h^2\mu_e^2B^2}B. \quad (5)$$

When contributions from both carrier types are significant, the Hall resistivity is nonlinear with B. Under sufficiently strong magnetic fields, however, the B-linear character is restored, with Eq. (5) reduced to

$$\rho_{yx}^{O} = \frac{1}{e}\frac{1}{n_h - n_e}B = \frac{1}{e}\frac{1}{n_{\text{eff}}}B, \quad (6)$$

with $n_{\text{eff}} = n_h - n_e$ being the effective carrier concentration. The second term in Eq. (4), $\rho_{xy}^{A}(M)$, is the anomalous component observed in magnetic materials. It may stem from side jump or skew scattering effects, or from the intrinsic Karplus-Luttinger mechanism involving the Berry curvature of the electronic bands [81]. Regardless of the underlying mechanism, this term is directly related to the sample magnetization.

In the temperature range far above T_N, where magnetization is not yet significant (see [78]), and $\rho_{xy}^{O} \gg \rho_{xy}^{A}$, Eq. (6) provides a first insight to the evolution of the carrier concentration. Figures 3(c) and 3(d) depict the thermal variation of n_{eff} obtained from the high-field limit of $\rho_{xy}(B)$. Because as $T \to T_N$, the high-field magnetization becomes more significant, in the vicinity of the magnetic ordering temperature Eq. (6) provides a less definitive measure of n_{eff}. Despite this limitation, the corresponding data, marked with shaded points in Figs. 3(c) and 3(d), can still be regarded as an useful guide.

In both compounds, n_{eff} exhibits a similar behavior; after a significant decrease, due to the opening of the CDW gap upon crossing the Peierls temperature, at approximately $\frac{T_P}{2}$, it becomes almost temperature-independent. This state remains until T starts to approach T_N, causing the continuous increase of the effective carrier concentration, which both in $HoNiC_2$ and $ErNiC_2$ reaches a maximum close to the magnetic ordering point and decreases again at the lowest temperature.

While the upturn in $n_{\text{eff}}(T)$ may be partially or even entirely caused by the finite anomalous Hall contribution as in Eq. (4), a conclusion can be drawn already from the fact that in both compounds $n_{\text{eff}}(T = 2\text{ K})$ attains a value lower than those observed at $T > T_P$. This effect is more pronounced in $ErNiC_2$, where n_{eff} never returns close to the levels measured at the highest temperatures, in the simple metallic state with no charge ordering. In $HoNiC_2$, the extremum of $n_{\text{eff}}(T)$ is more pronounced, yet after crossing T_N, its value sharply decreases and, similarly to the case of $ErNiC_2$, becomes significantly lower than in the high-temperature state. Even neglecting the anomalous Hall contribution and attributing this behavior directly to the evolution of the carrier concentration, the fact that $n_{\text{eff}}(T > T_P) \gg n_{\text{eff}}(T = 2\text{ K})$ indicates that the previously condensed carriers, or at least the majority of them, are not released when crossing T_N, but they remain gapped. According to the magnetic phase diagrams of $HoNiC_2$ and $ErNiC_2$ [55], n_{eff} probed at $T = 2$ K and applied field $\mu_0 H \to 9$ T corresponds already to the field-aligned ferromagnetic state. Therefore, this result not only confirms the coexistence of CDW and AFM order, as reported by Maeda *et al.* [36], but suggests that CDW survives in the entire magnetic domes of both compounds.

The nonlinearity of $\rho_{xy}(B)$ is however observed in a broad temperature range, exceeding the limit of $T \to T_N$. Therefore, next to the possible magnetization-dependent Hall resistivity contribution, this effect, and to some extent the increase of n_{eff} at low temperatures, suggests the presence of two contributions from different bands, including at least one of elevated mobility. The presence of electron and hole pockets is also in agreement with the maximum seen in the thermopower. Such a behavior in $S(T)$ can arise from bipolar flow of charged carriers, with their contributions being strongly temperature dependent.

Because of these visible signatures of charge compensation in $HoNiC_2$ and $ErNiC_2$, and due to long-range magnetic order being a part of both compounds' phase diagrams, it is favorable to use Hall conductivity $\sigma_{xy} = \frac{\rho_{yx}}{\rho_{yx}^2 + \rho_{xx}^2}$ for further analysis instead of resistivity to properly separate and discuss the relevant Hall effect counterparts. In such multiband systems with magnetic ordering, the overall Hall conductivity can be expressed using Eq. (7):

$$\sigma_{xy}(B) = \sigma_{xy}^{O}(B) + \sigma_{xy}^{A}(M) = \sum_i \frac{en_i\mu_i^2B}{1 + \mu_i^2B^2} + R_S\sigma_{xx}^{n}M. \quad (7)$$

The ordinary Hall conductivity $\sigma_{xy}^{O}(B)$ is the sum of the contributions stemming from i bands [80], with the carrier concentrations n_i and mobilities μ_i. The anomalous contribution $\sigma_{xy}^{A}(M)$ is proportional to magnetization M and moderated by diagonal conductance $\sigma_{xx} = \frac{\rho_{xx}}{\rho_{yx}^2 + \rho_{xx}^2}$ with the exponent n, depending on the underlying mechanism [81], and the coefficient R_S, being constant.

Each ith band's contribution to the ordinary counterpart of the Hall (off-diagonal) conductivity peaks when the magnetic field reaches the value equal to the inverse of μ_i. Each of the low-temperature $\sigma_{xy}(B)$ curves shows only a single maximum; thus the inverse of its position B_{ext} provides a measure of the dominant mobility, defined as [82]

$$\mu_{\text{ext}} = \frac{1}{B_{\text{ext}}}. \quad (8)$$

A complementary insight into the average electronic mobility μ_{MR} is provided also from the low-field limit of magnetoresistance [83], which can be derived directly by fitting $\text{MR}(B)|_{B\to 0}$ in Fig. 2 with

$$\frac{\rho_{xx}(B) - \rho_{xx}(B = 0)}{\rho_{xx}(B = 0)} \approx 1 + \mu_{\text{MR}}^2B^2. \quad (9)$$

The temperature dependence of the mobility obtained by both these approaches μ_{ext} and μ_{MR} is compared in Figs. 4(c) and 4(d). Despite the differences in the used models, the values of this quantity obtained with Eqs. (8) and (9) appear to be consistent with each other. Both compounds share a common character, with the mobility being almost temperature independent at high T and gradually increasing as temperature is lowered. To some extent, this behavior is reminiscent of the temperature dependence of both magnetoresistance and effective concentration (at low temperatures) shown in Figs. 1(e) and 1(f) and Figs. 3(c) and 3(d), suggesting that one band, presumably associated to a pocket generated by the imperfect

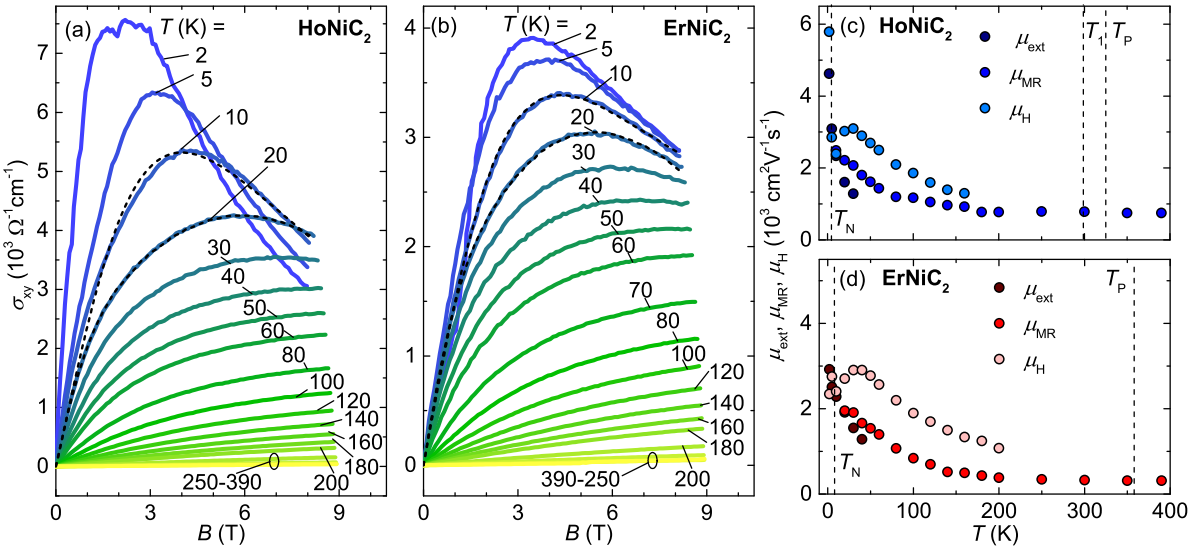

FIG. 4. (a), (b): Magnetic field dependence of Hall conductivity for $HoNiC_2$ (a) and $ErNiC_2$ (b). The temperature-color scheme, with colors varying from yellow for $T = 390$ K to dark blue for $T = 2$ K, is identical in panels (a) and (b). (c), (d): Temperature dependence of carrier mobility obtained with different methods for $HoNiC_2$ (c) and $ErNiC_2$ (d). μ_{ext} is obtained directly from the extremum position in $\sigma(B)$ curves, while μ_{MR} is estimated from the low-field magnetoresistance limit using Eq. (9) (see text and Supplemental Material [78] for details). Vertical dashed lines in panels (c) and (d) mark the charge density wave and magnetic transition temperatures.

Fermi surface nesting, is mainly responsible for the large magnetoresistance responses.

To follow the concentration and mobility of the carriers originating from this pocket, we use a model which takes into account one high-mobility band generating a single extremum in $\sigma_{xy}(B)$, and all the other bands, with significantly lower mobility, contributing a field-linear input [84]. In this model, we also include the anomalous Hall counterpart. Considering the relatively high longitudinal conductivity of the materials under study, being at the order of $\sigma_{xx} \sim 10^4\ \Omega^{-1}\,\mathrm{cm}^{-1}$, we conclude the intrinsic character of the Hall conductivity with $n = 0$ and anomalous Hall conductivity depending solely on magnetization, not on the scattering rate [85–87].

These two assumptions allow us to rewrite Eq. (7) as

$$\sigma_{xy}(B) = n_{\mathrm{H}} e \mu_{\mathrm{H}}^2 B \left(\frac{1}{1 + \mu_{\mathrm{H}}^2 B^2} + C \right) + S_A M, \qquad (10)$$

where n_{H} and μ_{H} are the concentration and mobility of the carriers representing the high-mobility band. The bands with lower mobility contribute to the parameter C. The anomalous Hall coefficient S_A for both compounds is obtained from a least-squares fit of the $T = 20$ K data and used for fits at different temperatures. Choosing this particular curve allows us to profit from the already pronounced curvature of the field-dependent magnetization, which facilitates the fitting procedure, and from the fact that this point lies outside of the dome of the magnetically ordered state. Therefore its possible impact on CDW and related carrier concentration is precluded. The obtained values of S_A yield 0.177 $\Omega\,\mathrm{A}^{-1}$ for $HoNiC_2$ and 0.131 $\Omega\,\mathrm{A}^{-1}$ for $ErNiC_2$, leading to a maximum anomalous Hall conductivity of $\sigma_{xy}^A \simeq 1.4 \times 10^3\ \Omega^{-1}\,\mathrm{cm}^{-1}$ ($HoNiC_2$) and $2.0 \times 10^3\ \Omega^{-1}\,\mathrm{cm}^{-1}$ ($ErNiC_2$), being consistent with the order of magnitude expected for the intrinsic origin of Hall conductivity [87].

The mobilities μ_{H} obtained from the fit are added to Figs. 4(c) and 4(d). In both compounds, μ_{H} shares a similar temperature dependence as μ_{MR} and μ_{ext}, obtained using different methods. The values of μ_{H} exceed μ_{MR} and μ_{ext} by less than $\approx 20\%$, underlining the consistency of the results obtained by three complementary models.

The most detailed approach, given in Eq. (10), captures also the local minimum in $\mu_{\mathrm{H}}(T)$, caused by the spin disorder scattering at the vicinity of T_N, locally decreasing the overall charge carrier mobility [88], and reflected in the temperature dependence of magnetoresistance [see Figs. 1(e) and 1(f)].

The thermal variation of high-mobility carrier concentration n_{H}, plotted in Figs. 3(c) and 3(d), is reminiscent of $n_{\mathrm{eff}}(T)$, suggesting that the pronounced upturn in the latter one may be partially contributed by the high-mobility band, which does not vanish at the lowest temperature. This finding further supports the scenario of charge order remaining not suppressed inside the magnetic dome.

IV. DIFFERENT BEHAVIORS OF q_1- AND q_2-CDW STATES

We find that the magnetotransport transport $HoNiC_2$ and $ErNiC_2$, both studied here, show close similarities with $YNiC_2$, $LuNiC_2$, and $TmNiC_2$ and remain in large contrast with $NdNiC_2$, $GdNiC_2$, and $SmNiC_2$. This underlines the major differences between these two groups, of which a common thread is the CDW order, yet the character of this state implies consequences, reaching far beyond the crystallographic point of view. The specific CDW order seen in these two parts of the family differ not only by the modulation vector [$q_1 = (0.5, 0.5 + \eta, 0.5)$ and $q_2 = (0.5, 0.5, 0.5)$, observed in early and late lanthanide based $RNiC_2$, respectively], point group symmetry breaking (q_2) or conserving (q_1), but also on the electronic band modifications inflicted by them and by the interactions with the long-range magnetic order.

The high mobility, as revealed in $HoNiC_2$ and $ErNiC_2$, is typically rooted at the electronic structure, as the carrier effective mass is governed by the band dispersion in the vicinity of the Fermi energy. The analysis of the band structure is thus essential to explain the origin of our experimental observations. The theoretical works on $RNiC_2$ predict the presence of an hourglass-shaped feature with steep, almost linear dispersion, reminiscent of a Dirac cone to be present close to the Fermi energy [89]. Interestingly, the relevant entity has been predicted to exist already in early-lanthanide based $RNiC_2$ [76,89–91], yet it is not continuously manifested in the evolution of transport properties on the path from light to heavy R element based $RNiC_2$ [76]. While the number of electrons per formula unit remains constant, the decrease of unit cell volume for heavier R based family members leads to a gradual change in the position of this feature in respect to the Fermi energy. A continuous increase of carrier mobility is therefore anticipated on the path from light to heavy lanthanide based $RNiC_2$. The experimental observations appear to be in contrast with this picture, pointing to another degree of freedom playing a crucial role in the magnetotransport response. Neither of the early lanthanide based $RNiC_2$, including those exhibiting the q_1-type CDW, shows any signatures of increased positive magnetoresistance, being a footprint of elevated mobility. This entity emerges suddenly and concomitantly with the transformation of q_1-CDW into the state represented by q_2 vector. Therefore, the presence of pronounced transport observables appears to be strongly related to the latter state. The comparison of the pristine and nested Fermi surface of $LuNiC_2$, exhibiting q_2-type CDW [39], indicates that while the majority of the FS is removed upon the Peierls transition, the part containing the Dirac-like feature is preserved and transforms into an hourglass-shaped FS element. Thus, our experimental observations result from a significant Fermi surface decomposition exposing the high-mobility pocket, which then dominates the transport picture. This mechanism gives rise to the behavior characteristic of compensated semimetals, with enhanced magnetotransport and thermoelectric responses, while it simultaneously conserves the high metallicity with residual resistivity on the order of tens of $\mu\Omega$ cm. While q_1-type CDW also leads to nesting-driven Fermi surface reconstruction, the lack of the high-mobility signatures in compounds showing this state suggests that the portion gapped in this process is significantly smaller than in the case of q_2-CDW.

The positive nonsaturating magnetoresistance term, appearing at the onset and accompanying only the q_2-CDW charge density wave, becomes its footprint, providing an useful probe to follow this state through the magnetic phase diagram. This finding exposes a crucial discrepancy between the response of the q_1- and q_2-CDW to the long-range magnetism. While the former CDW type suffers a partial or complete suppression at the onset of magnetic order, our analysis shows that the latter one, appearing in $HoNiC_2$ and $ErNiC_2$ under current study, shows no signatures of such a destructive interaction with magnetism, including antiferromagnetic ground state as well as the field-induced metamagnetic and field-aligned ferromagnetic states. Such a contrasting response to long-range magnetism is visible across the entire family, from the drop of resistivity at the onset of magnetically ordered state, as illustrated in Fig. 5. The values of RD observed in the $RNiC_2$ family exhibiting q_1-CDW, which are suppressed by magnetic ground state and the previously gapped carriers returning to conduction channels, are visibly larger than in the case of materials in which q_2-CDW is more robust and the resistivity drop is caused dominantly by the reduction of scattering rate.

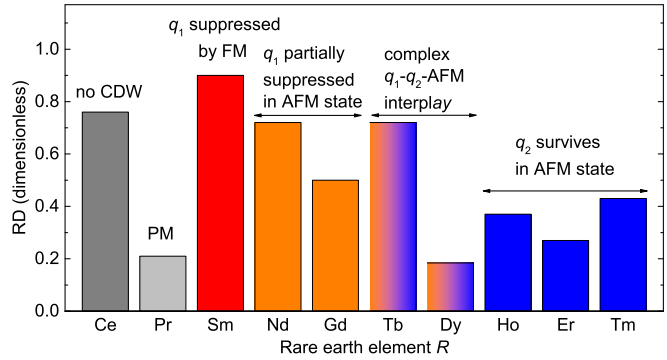

FIG. 5. Comparison of the resistivity drop RD, given by Eq. (1) at the onset of magnetic transition in all the $RNiC_2$ with magnetic order or short-range magnetic ordering, established in the current study and in Refs. [31,32,34,35,41,57]. Red color marks $SmNiC_2$ with q_1-CDW entirely suppressed by ferromagnetic order, yellow color is displayed for $RNiC_2$ members with q_1-type CDW partially suppressed by antiferromagnetism, blue color marks the $RNiC_2$ in which q_2-CDW is robust against long-range magnetic order. Cases of $CeNiC_2$ and $PrNiC_2$, showing no CDW ($CeNiC_2$) and paramagnetic (PM) ground state ($PrNiC_2$) are displayed in gray colors and serving as reference.

A plausible explanation of the divergent coupling between the electronic and magnetic degrees of freedom in q_1- and q_2-type systems is the difference in the mechanism driving the respective CDW transitions. The theoretical work devoted to the calculation of the electronic band structures of $NdNiC_2$, $SmNiC_2$, and $GdNiC_2$ [92] emphasizes the dominant role played by Fermi surface nesting in the formation of the q_1 charge density wave. This finding is supported by the continuous character and moderate specific heat anomaly accompanying the transition to this state in early lanthanide based $RNiC_2$ [93], consistent with a mean-field weak electron-phonon coupling scheme. In contrast to that, the band structure calculations performed for $LuNiC_2$, with q_2-type CDW, challenge the sole relevance of the conventional FS nesting for the charge density wave in this compound [39]. Further support for the strong electron-phonon coupling scenario proposed in Ref. [39] is provided by the large, spike-shaped anomaly in the specific heat, accompanying the q_2-CDW transition in $YNiC_2$ and $TmNiC_2$ [37,40], suggestive of the strong phonon influence on CDW formation. The strong Fermi surface reconstruction observed in these compounds, as well as $HoNiC_2$ and $ErNiC_2$ studied here, therefore appears to be a consequence rather than the origin of the CDW transition.

Since the q_1-CDW in early lanthanide-based $RNiC_2$ relies mostly on the FS nesting, this state becomes vulnerable to the evolution of the electronic structure. The spin-orbit interaction induced splitting of the conduction bands may then directly

lead to the suppression of nesting properties and a consequent destruction of the charge density wave. Such a mechanism has been proposed for the case of $SmNiC_2$ [89], in which the energy scale of the band splitting in the ferromagnetic state surpasses even the magnitude of the charge density wave gap [94]. In contrast to that, the q_2 state which is presumably stabilized by a distinct mechanism, independent of the minute details of the electronic structure, resists the spin-splitting induced deterioration of the nesting properties and survives in the entire dome of magnetically ordered states.

V. CONCLUSIONS

We have examined the diagonal and off-diagonal components of the transport responses in $HoNiC_2$ and $ErNiC_2$. Both compounds show large positive and linear magnetoresistance which neither saturates in the high-field limit nor vanishes across the temperature and field-induced magnetic transitions. We find that this effect originates from the compensated transport picture comprising at least two conduction bands, including one with high mobility reaching 3×10^3 cm^2 V^{-1} s^{-1}. This effect is attributed to the incomplete Fermi surface nesting giving rise to the high-mobility pockets. This mechanism, bringing both systems closer to compensated semimetals comprising both electron and hole conduction channels, is responsible also for relatively high thermoelectric output, observed within the boundary of a highly conducting metallic state. The robustness of these pockets in the magnetically ordered phase, as revealed by the Hall effect and persistence of a high-field large linear magnetoresistance, together with the absence of other signatures of CDW suppression, such as the avalanche of negative magnetoresistance at the ferromagnetic transition, suggests that the charge ordering coexists with all the magnetic phases present in the phase diagrams of $HoNiC_2$ and $ErNiC_2$ from antiferromagnetic to field-induced ferromagnetic states.

ACKNOWLEDGMENTS

The project is cofinanced by a bilateral project of the Polish National Agency for Academic Exchange Grant PPN/BAT/2021/1/00016, and Austrian Academic Exchange Service ÖAD Grant PL04/2022. M.R. acknowledges the financial support by Grant No. DEC-08/2021/IDUB/II.1/AMERICIUM of the AMERICIUM "Excellence Initiative-Research University" Program of the Gdansk University of Technology. The authors would also like to thank to Jesse D. Sprowes for his helpful comments.

[1] H. Fröhlich, On the theory of superconductivity: The one-dimensional case, Proc. R. Soc. London A **223**, 296 (1954).
[2] R. E. Peierls, *Quantum Theory of Solids* (Oxford University Press, Oxford, UK, 1955).
[3] Z. Wang, M. Saint-Lager, P. Monceau, M. Renard, P. Gressier, A. Meerschaut, L. Guemas, and J. Rouxel, Charge density wave transport in $(TaSe_4)_2I$, Solid State Commun. **46**, 325 (1983).
[4] G. H. J. Bouchard, J. H. Perlstein, and M. J. Sienko, Solid-state studies of potassium molybdenum bronzes, Inorg. Chem. **6**, 1682 (1967).
[5] J. P. Pouget, S. Kagoshima, C. Schlenker, and J. Marcus, Evidence for a Peierls transition in the blue bronzes $K_{0.30}MoO_3$ and $Rb_{0.30}MoO_3$, J. Phys. Lett. **44**, 113 (1983).
[6] H. Guyot, C. Schlenker, G. Fourcaudot, and K. Konaté, Charge density wave instability in the quasi two-dimensional metal γ-Mo_4O_{11}, Solid State Commun. **54**, 909 (1985).
[7] C. W. Chu, J. M. E. Harper, T. H. Geballe, and R. L. Greene, Pressure dependence of the metal-insulator transition in tetrathiofulvalinium tetracyanoquinodimethane (TTF-TCNQ), Phys. Rev. Lett. **31**, 1491 (1973).
[8] D. Jérome, W. Müller, and M. Weger, Pressure investigation of the metal-semiconductor transition in TTF-TCNQ, J. Phys. Lett. **35**, 77 (1974).
[9] G. Grüner, The dynamics of charge-density waves, Rev. Mod. Phys. **60**, 1129 (1988).
[10] G. Grüner, *Density Waves in Solids* (CRC Press, Boca Raton, FL, USA, 1994).
[11] P. Monceau, Electronic crystals: An experimental overview, Adv. Phys. **61**, 325 (2012).
[12] J. Chaussy, P. Haen, J. Lasjaunias, P. Monceau, G. Waysand, A. Waintal, A. Meerschaut, P. Molinié, and J. Rouxel, Phase transitions in $NbSe_3$, Solid State Commun. **20**, 759 (1976).
[13] J. L. Hodeau, M. Marezio, C. Roucau, R. Ayroles, A. Meerschaut, J. Rouxel, and P. Monceau, Charge-density waves in $NbSe_3$ at 145 K: Crystal structures, x-ray and electron diffraction studies, J. Phys. C **11**, 4117 (1978).
[14] J.-S. Rhyee, K. H. Lee, S. M. Lee, E. Cho, S. I. Kim, E. Lee, Y. S. Kwon, J. H. Shim, and G. Kotliar, Peierls distortion as a route to high thermoelectric performance in $In_4Se_{3-\delta}$ crystals, Nature (London) **459**, 965 (2009).
[15] H. Cho, J. H. Yun, J. H. Kim, S. Y. Back, H. S. Lee, S. J. Kim, S. Byeon, H. Jin, and J.-S. Rhyee, Possible charge density wave and enhancement of thermoelectric properties at mild-temperature range in n-type CuI-doped $Bi_2Te_{2.1}Se_{0.9}$ compounds, ACS Appl. Mater. Interfaces **12**, 925 (2020).
[16] C. Hess, C. Schlenker, J. Dumas, M. Greenblatt, and Z. S. Teweldemedhin, Magnetotransport and thermopower properties of the quasi-two-dimensional charge-density-wave compounds $(PO_2)_4(WO_3)_{2m}$ ($m = 4, 6$), Phys. Rev. B **54**, 4581 (1996).
[17] M.-L. Tian, S. Yue, S. Li, Y. Zhang, and J. Shi, Magnetoresistance properties of quasi-two-dimensional charge-density wave compounds AMo_6O_{17} (A = Na, K, and Tl), J. Appl. Phys. **89**, 3408 (2001).
[18] M. Tian, S. Yue, and Y. Zhang, Magnetoresistance of quasi-two-dimensional purple bronzes AMo_6O_{17} (A = Na, K, and Tl), Phys. Rev. B **65**, 104421 (2002).
[19] V. K. Joshi, Spintronics: A contemporary review of emerging electronics devices, Eng. Sci. Technol. Int. J. **19**, 1503 (2016).
[20] W. Chen, J. George, J. B. Varley, G.-M. Rignanese, and G. Hautier, High-throughput computational discovery of $In_2Mn_2O_7$ as a high Curie temperature ferromagnetic semiconductor for spintronics, npj Comput. Mater. **5**, 72 (2019).
[21] S. Lei, J. Lin, Y. Jia, M. Gray, A. Topp, G. Farahi, S. Klemenz, T. Gao, F. Rodolakis, J. L. McChesney, C. R. Ast, A. Yazdani,

K. S. Burch, S. Wu, N. P. Ong, and L. M. Schoop, High mobility in a van der Waals layered antiferromagnetic metal, Sci. Adv. **6**, eaay6407 (2020).

[22] Y. He, J. Gayles, M. Yao, T. Helm, T. Reimann, V. N. Strocov, W. Schnelle, M. Nicklas, Y. Sun, G. H. Fecher, and C. Felser, Large linear non-saturating magnetoresistance and high mobility in ferromagnetic MnBi, Nat. Commun. **12**, 4576 (2021).

[23] S. Kawasaki, Z. Li, M. Kitahashi, C. T. Lin, P. L. Kuhns, A. P. Reyes, and G.-q. Zheng, Charge-density-wave order takes over antiferromagnetism in $Bi_2Sr_{2-x}La_xCuO_6$ superconductors, Nat. Commun. **8**, 1267 (2017).

[24] P. M. Coelho, K. Nguyen Cong, M. Bonilla, S. Kolekar, M.-H. Phan, J. Avila, M. C. Asensio, I. I. Oleynik, and M. Batzill, Charge density wave state suppresses ferromagnetic ordering in VSe_2 monolayers, J. Phys. Chem. C **123**, 14089 (2019).

[25] S. Ramakrishnan, A. Schönleber, T. Rekis, N. van Well, L. Noohinejad, S. van Smaalen, M. Tolkiehn, C. Paulmann, B. Bag, A. Thamizhavel, D. Pal, and S. Ramakrishnan, Unusual charge density wave transition and absence of magnetic ordering in $Er_2Ir_3Si_5$, Phys. Rev. B **101**, 060101(R) (2020).

[26] F. Galli, R. Feyerherm, R. W. A. Hendrikx, E. Dudzik, G. J. Nieuwenhuys, S. Ramakrishnan, S. D. Brown, S. van Smaalen, and J. A. Mydosh, Coexistence of charge density wave and antiferromagnetism in $Er_5Ir_4Si_{10}$, J. Phys.: Condens. Matter **14**, 5067 (2002).

[27] X. Teng, L. Chen, F. Ye, E. Rosenberg, Z. Liu, J.-X. Yin, Y.-X. Jiang, J. S. Oh, M. Z. Hasan, K. J. Neubauer, B. Gao, Y. Xie, M. Hashimoto, D. Lu, C. Jozwiak, A. Bostwick, E. Rotenberg, R. J. Birgeneau, J.-H. Chu, M. Yi *et al.*, Discovery of charge density wave in a kagome lattice antiferromagnet, Nature (London) **609**, 490 (2022).

[28] X. Teng, J. S. Oh, H. Tan, L. Chen, J. Huang, B. Gao, J.-X. Yin, J.-H. Chu, M. Hashimoto, D. Lu, C. Jozwiak, A. Bostwick, E. Rotenberg, G. E. Granroth, B. Yan, R. J. Birgeneau, P. Dai, and M. Yi, Magnetism and charge density wave order in kagome FeGe, Nat. Phys. **19**, 814 (2023).

[29] J. Zhou, Z. Wang, S. Wang, Y. P. Feng, M. Yang, and L. Shen, Coexistence of ferromagnetism and charge density waves in monolayer $LaBr_2$, Nanoscale Horiz. **8**, 1054 (2023).

[30] A. Wölfel, L. Li, S. Shimomura, H. Onodera, and S. van Smaalen, Commensurate charge-density wave with frustrated interchain coupling in $SmNiC_2$, Phys. Rev. B **82**, 054120 (2010).

[31] N. Yamamoto, R. Kondo, H. Maeda, and Y. Nogami, Interplay of charge-density wave and magnetic order in ternary rare-earth nickel carbides, $RNiC_2$ (R = Pr and Nd), J. Phys. Soc. Jpn. **82**, 123701 (2013).

[32] H. Lei, K. Wang, and C. Petrovic, Magnetic-field-tuned charge density wave in $SmNiC_2$ and $NdNiC_2$, J. Phys.: Condens. Matter **29**, 075602 (2017).

[33] N. Hanasaki, S. Shimomura, K. Mikami, Y. Nogami, H. Nakao, and H. Onodera, Interplay between charge density wave and antiferromagnetic order in $GdNiC_2$, Phys. Rev. B **95**, 085103 (2017).

[34] S. Shimomura, C. Hayashi, G. Asaka, N. Wakabayashi, M. Mizumaki, and H. Onodera, Charge-density-wave destruction and ferromagnetic order in $SmNiC_2$, Phys. Rev. Lett. **102**, 076404 (2009).

[35] N. Hanasaki, Y. Nogami, M. Kakinuma, S. Shimomura, M. Kosaka, and H. Onodera, Magnetic field switching of the charge-density-wave state in the lanthanide intermetallic $SmNiC_2$, Phys. Rev. B **85**, 092402 (2012).

[36] H. Maeda, R. Kondo, and Y. Nogami, Multiple charge density waves compete in ternary rare-earth nickel carbides, $RNiC_2$ (R: Y, Dy, Ho, and Er), Phys. Rev. B **100**, 104107 (2019).

[37] M. Roman, M. Fritthum, B. Stöger, D. T. Adroja, and H. Michor, Charge density wave and crystalline electric field effects in $TmNiC_2$, Phys. Rev. B **107**, 125137 (2023).

[38] M. Roman, J. Strychalska-Nowak, T. Klimczuk, and K. K. Kolincio, Extended phase diagram of $RNiC_2$ family: Linear scaling of the Peierls temperature, Phys. Rev. B **97**, 041103(R) (2018).

[39] S. Steiner, H. Michor, O. Sologub, B. Hinterleitner, F. Höfenstock, M. Waas, E. Bauer, B. Stöger, V. Babizhetskyy, V. Levytskyy, and B. Kotur, Single-crystal study of the charge density wave metal $LuNiC_2$, Phys. Rev. B **97**, 205115 (2018).

[40] K. K. Kolincio, M. Roman, and T. Klimczuk, Charge density wave and large nonsaturating magnetoresistance in $YNiC_2$ and $LuNiC_2$, Phys. Rev. B **99**, 205127 (2019).

[41] K. K. Kolincio, M. Roman, and T. Klimczuk, Enhanced mobility and large linear nonsaturating magnetoresistance in the magnetically ordered states of $TmNiC_2$, Phys. Rev. Lett. **125**, 176601 (2020).

[42] P. Kotsanidis, J. Yakinthos, and E. Gamari-Seale, Magnetic properties of the ternary carbides of the rare earth and nickel group metals, J. Less-Common Met. **152**, 287 (1989).

[43] F. Garmroudi, M. Parzer, M. Knopf, A. Riss, H. Michor, A. V. Ruban, T. Mori, and E. Bauer, Unveiling the structure-property relationship in metastable Heusler compounds by systematic disorder tuning, Phys. Rev. B **107**, 014108 (2023).

[44] J. A. Osborn, Demagnetizing factors of the general ellipsoid, Phys. Rev. **67**, 351 (1945).

[45] R. Resel, E. Gratz, A. T. Burkov, T. Nakama, M. Higa, and K. Yagasaki, Thermopower measurements in magnetic fields up to 17 tesla using the toggled heating method, Rev. Sci. Instrum. **67**, 1970 (1996).

[46] S. Iwanaga, E. S. Toberer, A. LaLonde, and G. J. Snyder, A high temperature apparatus for measurement of the Seebeck coefficient, Rev. Sci. Instrum. **82**, 063905 (2011).

[47] J. de Boor, C. Stiewe, P. Ziolkowski, T. Dasgupta, G. Karpinski, E. Lenz, F. Edler, and E. Mueller, High-temperature measurement of Seebeck coefficient and electrical conductivity, J. Electron. Mater. **42**, 1711 (2013).

[48] G. Saunders, C. Miziumski, G. Cooper, and A. Lawson, The Seebeck coefficients of antimony and arsenic single crystals, J. Phys. Chem. Solids **26**, 1299 (1965).

[49] D. Rowe, *Thermoelectrics Handbook: Macro to Nano* (CRC Press, Boca Raton, FL, USA, 2006).

[50] B. Saparov, J. E. Mitchell, and A. S. Sefat, Properties of binary transition-metal arsenides (TAs), Supercond. Sci. Technol. **25**, 084016 (2012).

[51] J. H. Kim, J.-S. Rhyee, and Y. S. Kwon, Magnon gap formation and charge density wave effect on thermoelectric properties in the $SmNiC_2$ compound, Phys. Rev. B **86**, 235101 (2012).

[52] K. K. Kolincio, K. Górnicka, M. J. Winiarski, J. Strychalska-Nowak, and T. Klimczuk, Field-induced suppression of charge density wave in $GdNiC_2$, Phys. Rev. B **94**, 195149 (2016).

[53] K. K. Kolincio, M. Roman, M. J. Winiarski, J. Strychalska-Nowak, and T. Klimczuk, Magnetism and charge density waves in $RNiC_2$ (R = Ce, Pr, Nd), Phys. Rev. B **95**, 235156 (2017).

[54] J. Yakinthos, P. Kotsanidis, W. Schäfer, and G. Will, Magnetic structure determination of $NdNiC_2$ and $TmNiC_2$ by neutron diffraction, J. Magn. Magn. Mater. **89**, 299 (1990).

[55] Y. Koshikawa, H. Onodera, M. Kosaka, H. Yamauchi, M. Ohashi, and Y. Yamaguchi, Crystalline electric fields and magnetic properties of single-crystalline $RNiC_2$ compounds (R = Ho, Er and Tm), J. Magn. Magn. Mater. **173**, 72 (1997).

[56] H. Michor, S. Steiner, A. Schumer, M. Hembara, V. Levytskyy, V. Babizhetskyy, and B. Kotur, Magnetic properties of $HoCoC_2$, $HoNiC_2$ and their solid solutions, J. Magn. Magn. Mater. **441**, 69 (2017).

[57] S. Shimomura, C. Hayashi, N. Hanasaki, K. Ohnuma, Y. Kobayashi, H. Nakao, M. Mizumaki, and H. Onodera, Multiple charge density wave transitions in the antiferromagnets $RNiC_2$ (R = Gd, Tb), Phys. Rev. B **93**, 165108 (2016).

[58] N. P. Ong and J. W. Brill, Conductivity anisotropy and transverse magnetoresistance of $NbSe_3$, Phys. Rev. B **18**, 5265 (1978).

[59] M. Naito and S. Tanaka, Galvanomagnetic effects in the charge-density-wave state of 2H-$NbSe_2$ and 2H-$TaSe_2$, J. Phys. Soc. Jpn. **51**, 228 (1982).

[60] J. He, L. Wen, Y. Wu, J. Liu, G. Tang, Y. Yang, H. Xing, Z. Mao, H. Sun, and Y. Liu, Angle-dependent magnetoresistance as a sensitive probe of the charge density wave in quasi-one-dimensional semimetal Ta_2NiSe_7, Appl. Phys. Lett. **113**, 192401 (2018).

[61] M.-H. Whangbo, E. Canadell, P. Foury, and J. P. Pouget, Hidden Fermi surface nesting and charge density wave instability in low-dimensional metals, Science **252**, 96 (1991).

[62] J. Dumas and C. Schlenker, Charge density wave properties of molybdenum bronzes, Int. J. Mod. Phys. B **07**, 4045 (1993).

[63] H. Balaska, J. Dumas, H. Guyot, P. Mallet, J. Marcus, C. Schlenker, J. Veuillen, and D. Vignolles, Charge density wave properties of the quasi two-dimensional purple molybdenum bronze KMo_6O_{17}, Solid State Sci. **7**, 690 (2005).

[64] H. P. Zhu, M. Yang, J. Z. Ke, H. K. Zuo, T. Peng, J. F. Wang, Y. Liu, X. Xu, Y. Kohama, K. Kindo, and M. Greenblatt, Quantum oscillations and magnetic field induced Fermi surface reconstruction in the charge density wave state of $A_{0.9}Mo_6O_{17}$, Phys. Rev. B **102**, 235164 (2020).

[65] A. Rötger, J. Lehmann, C. Schlenker, J. Dumas, J. Marcus, Z. S. Teweldemedhin, and M. Greenblatt, Magnetotransport properties in the charge density wave state of the quasi-two-dimensional compounds $(PO_2)_4(WO_3)_{2m}$, Europhys. Lett. **25**, 23 (1994).

[66] M. Greenblatt, Molybdenum and tungsten bronzes, in *Physics and Chemistry of Low-Dimensional Inorganic Conductors*, edited by C. Schlenker, J. Dumas, M. Greenblatt, and S. van Smaalen (Springer US, Boston, MA, 1996), pp. 15–43.

[67] S. Drouard, P. Foury, P. Roussel, D. Groult, J. Dumas, J. Pouget, and C. Schlenker, Coupled electronic and structural transition in the quasi two-dimensional conductors $K_xP_4W_8O_{32}$, Synth. Met. **103**, 2636 (1999).

[68] Y. Moritomo, A. Asamitsu, H. Kuwahara, and Y. Tokura, Giant magnetoresistance of manganese oxides with a layered perovskite structure, Nature (London) **380**, 141 (1996).

[69] B. Raveau, A. Maignan, C. Martin, and M. Hervieu, Colossal magnetoresistance manganite perovskites: Relations between crystal chemistry and properties, Chem. Mater. **10**, 2641 (1998).

[70] Y. Feng, Y. Wang, D. M. Silevitch, J.-Q. Yan, R. Kobayashi, M. Hedo, T. Nakama, Y. Onuki, A. V. Suslov, B. Mihaila, P. B. Littlewood, and T. F. Rosenbaum, Linear magnetoresistance in the low-field limit in density-wave materials, Proc. Natl. Acad. Sci. USA **116**, 11201 (2019).

[71] A. A. Sinchenko, P. D. Grigoriev, P. Lejay, and P. Monceau, Linear magnetoresistance in the charge density wave state of quasi-two-dimensional rare-earth tritellurides, Phys. Rev. B **96**, 245129 (2017).

[72] M. M. Parish and P. B. Littlewood, Non-saturating magnetoresistance in heavily disordered semiconductors, Nature (London) **426**, 162 (2003).

[73] A. A. Abrikosov, Quantum magnetoresistance, Phys. Rev. B **58**, 2788 (1998).

[74] A. A. Abrikosov, Quantum linear magnetoresistance, Europhys. Lett. **49**, 789 (2000).

[75] A. B. Pippard, *Magnetoresistance in Metals* (Cambridge University Press, Cambridge, UK, 1989).

[76] R. Ray, B. Sadhukhan, M. Richter, J. I. Facio, and J. van den Brink, Tunable chirality of noncentrosymmetric magnetic Weyl semimetals in rare-earth carbides, npj Quantum Mater. **7**, 19 (2022).

[77] C. Shekhar, A. K. Nayak, Y. Sun, M. Schmidt, M. Nicklas, I. Leermakers, U. Zeitler, Y. Skourski, J. Wosnitza, Z. Liu, Y. Chen, W. Schnelle, H. Borrmann, Y. Grin, C. Felser, and B. Yan, Extremely large magnetoresistance and ultrahigh mobility in the topological Weyl semimetal candidate NbP, Nat. Phys. **11**, 645 (2015).

[78] See Supplemental Material at http://link.aps.org/supplemental/10.1103/PhysRevB.109.075154 for magnetization data and further details and descriptions of the used methods.

[79] L. Berger and G. Bergmann, The Hall effect of ferromagnets, in *The Hall Effect and Its Applications*, edited by C. L. Chien and C. R. Westgate (Springer US, Boston, MA, 1980), pp. 55–76.

[80] C. M. Hurd, *The Hall Effect in Metals and Alloys* (Springer, New York, 1972).

[81] N. Nagaosa, J. Sinova, S. Onoda, A. H. MacDonald, and N. P. Ong, Anomalous Hall effect, Rev. Mod. Phys. **82**, 1539 (2010).

[82] T. Liang, Q. Gibson, M. N. Ali, M. Liu, R. J. Cava, and N. P. Ong, Ultrahigh mobility and giant magnetoresistance in the Dirac semimetal Cd_3As_2, Nat. Mater. **14**, 280 (2015).

[83] D. E. Soule, Magnetic field dependence of the Hall effect and magnetoresistance in graphite single crystals, Phys. Rev. **112**, 698 (1958).

[84] H. Takahashi, R. Okazaki, Y. Yasui, and I. Terasaki, Low-temperature magnetotransport of the narrow-gap semiconductor $FeSb_2$, Phys. Rev. B **84**, 205215 (2011).

[85] R. Karplus and J. M. Luttinger, Hall effect in ferromagnetics, Phys. Rev. **95**, 1154 (1954).

[86] S. Onoda, N. Sugimoto, and N. Nagaosa, Intrinsic versus extrinsic anomalous Hall effect in ferromagnets, Phys. Rev. Lett. **97**, 126602 (2006).

[87] S. Onoda, N. Sugimoto, and N. Nagaosa, Quantum transport theory of anomalous electric, thermoelectric, and thermal Hall effects in ferromagnets, Phys. Rev. B **77**, 165103 (2008).

[88] C. Haas, Spin-disorder scattering and magnetoresistance of magnetic semiconductors, Phys. Rev. **168**, 531 (1968).

[89] J. N. Kim, C. Lee, and J.-H. Shim, Chemical and hydrostatic pressure effect on charge density waves of $SmNiC_2$, New J. Phys. **15**, 123018 (2013).

[90] Y. Zhang, T. Usman, X.-m. Tao, and M.-q. Tan, A first-principle calculation and de Haas-van Alphen effect simulation in superconductor $LaNiC_2$, J. Supercond. Novel Magn. **31**, 995 (2018).

[91] I. Hase and T. Yanagisawa, Electronic structure of $RNiC_2$ (R = La, Y, and Th), J. Phys. Soc. Jpn. **78**, 084724 (2009).

[92] J. Laverock, T. D. Haynes, C. Utfeld, and S. B. Dugdale, Electronic structure of $RNiC_2$ (R = Sm, Gd, and Nd) intermetallic compounds, Phys. Rev. B **80**, 125111 (2009).

[93] M. Murase, A. Tobo, H. Onodera, Y. Hirano, T. Hosaka, S. Shimomura, and N. Wakabayashi, Lattice constants, electrical resistivity and specific heat of $RNiC_2$, J. Phys. Soc. Jpn. **73**, 2790 (2004).

[94] T. Sato, S. Souma, K. Nakayama, T. Takahashi, S. Shimomura, and H. Onodera, Pseudogap of charge-density-wave compound $SmNiC_2$ studied by high-resolution photoemission spectroscopy, J. Phys. Soc. Jpn. **79**, 044707 (2010).